buildings

MDPI

Article

Push-Out Analysis on the Shear Performance of a New Type of Bellow-Sleeved Stud

Disheng Zou [1], Qingtian Su [1,2], Fei Wu [1,*], Zhiping Lin [3] and Peiran Li [4]

[1] Department of Bridge Engineering, Tongji University, Shanghai 200092, China; 2232574@tongji.edu.cn (D.Z.)
[2] Shanghai Engineering Research Center of High Performance Composite Bridge, Shanghai 200092, China
[3] Fujian Expressway Group Co., Ltd., Fuzhou 350001, China
[4] Henan Transportation Planning and Design Research Institute Co., Ltd., Zhengzhou 450008, China
* Correspondence: 1810754@tongji.edu.cn

Abstract: For continuous steel–concrete composite girder bridges based on the post-combined method, the conventional rectangular group studs contribute to the isolation of the steel girder and the concrete slab before prestressing, leading to the majority of prestress forces being introduced to the concrete slab. However, rectangular-group stud holes cause the prestress forces to be unevenly distributed. In this study, a new type of bellow-sleeved stud (BSS) was developed to mitigate the weakening effects of rectangular group stud holes on the slab. A steel corrugated sleeve with a diameter of 60 mm was employed to cover the stud, which served as an internal formwork to prevent the concrete from bonding with the root of the stud. After prestressing was complete, the steel sleeve was filled with ultra-high-performance concrete (UHPC) to create a reliable combination between the concrete slab and the steel girder. To investigate the shear performance of this new type of connection, eight push-out test specimens were designed, and finite-element models were built. This study drew a comparison between the BSS and the ordinary headed stud (OHS). The research findings suggested that the BSS is subjected to less bending–shear coupling and offers a 4.5% increase in shear strength and a 31.9% increase in shear stiffness compared with the OHS. The study also analyzed the structural parameters influencing the shear performance of the BSS. It is found that the steel sleeve of the BSS has a negative effect on shear performance, but this can be mitigated by infusing high-strength material into the sleeve. Furthermore, the study examined the effect of construction quality on shear performance and suggested that sleeve deviation and grout leakage considerably reduced the shear performance of the BSS. Accordingly, strict control over the construction quality of the BSS is necessary.

Keywords: bellow-sleeved stud; shear performance; push-out test; post-combined prestressing method

Citation: Zou, D.; Su, Q.; Wu, F.; Lin, Z.; Li, P. Push-Out Analysis on the Shear Performance of a New Type of Bellow-Sleeved Stud. *Buildings* **2024**, *14*, 1483. https://doi.org/10.3390/buildings14051483

Academic Editor: Nerio Tullini

Received: 20 March 2024
Revised: 10 May 2024
Accepted: 13 May 2024
Published: 20 May 2024

1. Introduction

The shear connector in the steel–concrete composite girder bridge tightly combines the concrete bridge deck with the steel main girder together to resist the effects of external loads. These connectors not only transmit the horizontal shear force along the steel–concrete interface, but also resist the vertical separation between steel and concrete [1]. Welded studs, i.e., a type of flexible connector commonly used in bridge engineering, exhibit isotropic shear resistance and can be uniformly distributed across distinct regions. Since 1956, a significant number of the push-out tests have been performed, so that several empirical formulas for effective shear capacity and elastic shear stiffness have been derived [2–5]. In 1985, Roik [6] conducted reliability analysis on the shear capacity of studs and recommended the adoption of a partial factor γ_v = 1.25 for stud design, which is an approach that was approved from the EN1990 standard [7] and has since been continuously employed. After decades of development, the design method of the individual shear stud has been clearly specified in the current codal provisions or guidelines across the world [8–10].

After 1990, there have been continual breakthroughs in the new technology of prestressed composite girder bridges [11–14], leading to innovative changes to the construction form and the arrangement of shear studs. In order to enhance the efficiency of prestressing in continuous composite girder bridges, Su Hang introduced the partial-combined method [15] and proposed a new type of rubber-sleeved stud (RSS) [16]. The principle of this method involves utilizing the extrusion of the rubber sleeve to minimize the shear stiffness of the stud, allowing the majority of precompression stress to be transmitted into the slab. Experimental studies indicate that the initial shear stiffness of the RSS decreases to 1% of ordinary headed studs (OHSs), achieving a prestress transfer efficiency of 95%. Simultaneously, Su [17] proposed the post-combined prestressing method, which arranges the shear studs in groups in the negative moment region, ensuring isolation between the slab and the steel girder before prestressing. Initially, prestressed tendons are tensioned to direct all prestress into the concrete bridge slab. Next, high-strength mortar is employed for secondary casting in the reserved group stud holes, such that the concrete bridge slab is combined with the steel girder.

To research the shear behavior of the group studs applied to the post-combined method, Xue [18] conducted push-out tests and found that the group effect reduces the shear performance of the stud, necessitating the introduction of a reduction factor in the design. Yu [19] analyzed the stiffness of the group studs based on the Winkler foundation model, deriving a theoretical calculation formula considering the concrete material, stud diameter, and the number of shear studs. These research indicates that the shear performance of the group studs meets the requirement of the post-combined prestressing method. However, according to onsite testing, Su [20] suggested that the traditional rectangular-group stud holes on the post-combined slab exert a pronounced weakening effect. The precompression stress generated by prestressing tendons cannot be uniformly transferred into the bridge deck, causing stress to be unevenly distributed across the width of the bridge deck. The precompression stress between two consecutive group stud holes was 1.4 MPa, much lower than the average prestress of 10.3 MPa inside the concrete slab.

To ameliorate the uneven distribution of the prestress force, this study proposed a new type of bellow-sleeved stud (BSS). A steel corrugated sleeve with a diameter of 60 mm was employed to cover the stud, which served as an internal formwork to prevent the concrete from bonding with the root of the stud. After prestressing was complete, the steel sleeve was filled with ultra-high-performance concrete (UHPC) to create a reliable combination between the concrete bridge slab and the steel girder. Research found that the BBS increases the precompression stress between two consecutive group stud holes to 7.8 MPa, but its shear performance is still unknown. Differing from the conventional group studs, the steel sleeve is positioned close to the root of the stud, and a significant contrast exists in characteristics between the materials inside and outside the steel sleeve (UHPC inside the sleeve, ordinary concrete outside the sleeve). In this case, the shear performance of this new type of stud has hardly been evaluated by previous research and the current design code. Consequently, push-out tests and numerical studies should be conducted on the BSS to explore its shear mechanism.

2. Push-Out Test

2.1. Specimen Design

In this study, eight pieces of push-out specimens were developed to examine the shear performance of this new type of shear stud, with the characteristics of these specimens listed in Table 1. The type of shear stud was involved in the variation in specimens. OHS and BSS represent the standard push-out specimens welded with ordinary headed studs and bellow-sleeved studs, respectively. Since the construction equality has a considerable influence on the test results, the number of the specimen BSS was set as 5.

Table 1. Characteristics of the test specimen.

Specimen ID	Stud Dimension (Diameter × Height)	Stud Arrangement (Single-Side)	Bellow Dimension (Diameter × Height)	Material Inside Bellow	Number
OHS	22 × 200	1 × 2	NA	NA	3
BSS	22 × 200	1 × 2	60 × 320	UHPC	5

Figure 1 depicts the specimen and the reinforcement layout. Each specimen was developed following the same dimensions, while the only difference in all specimens lay in the type of shear stud. The test piece was cast with C50 concrete characterized by a thickness of 320 mm and then reinforced by HRB400 steel bar possessing a diameter of 20 mm, consistent with the practical bridge slab. The ML15 headed stud, which has been extensively employed in bridge engineering, was selected as the test subject, with a diameter and height of 22 mm and 200 mm, respectively. The bellow buried in BSS was constituted by a steel corrugated sleeve, which exhibited a diameter of 60 mm and a length of 320 mm. Moreover, UHPC served as the grout in the bellow, which was cast after the concrete outside was completed following the casting sequence of the bridge slab based on the post-combined prestressing method.

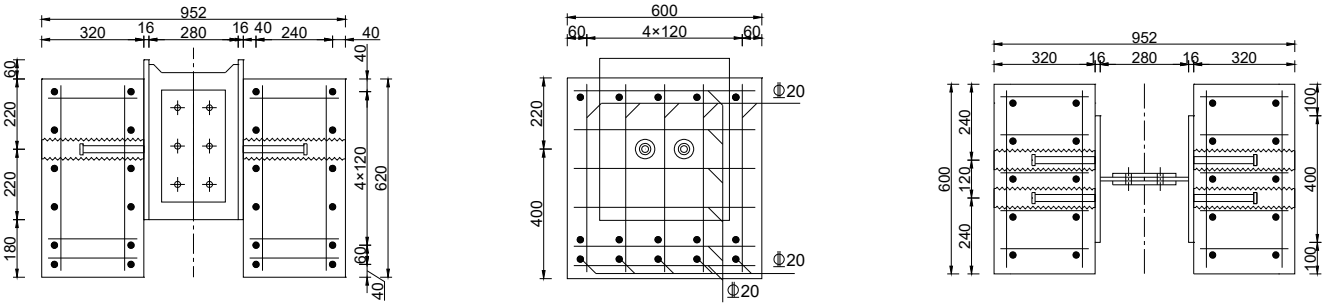

(**a**) Front view (**b**) Side view (**c**) Top view

Figure 1. Specimen and the reinforcement layout of BSS.

The H-shaped steel structure of the specimen was connected by two T-shaped steel plates through bolts. The flange exhibited a thickness of 16 mm, and the respective flange was welded with two headed studs symmetrically centered on the web plate, creating a transverse spacing of 120 mm. Thus, the pushing force was distributed uniformly to four shear studs buried in the specimen, such that this force was not concentrated on the single headed stud.

Figure 2 shows the construction process of the specimen BSS. The respective specimen comprised two identical parts fabricated by lying on the ground. After the shear studs were welded on the outer surface of the steel flange, the interaction surface on the flange was coated with engine oil, with the aim of reducing the friction between steel and concrete. As a result, the test result can be less affected. Subsequently, the framework was erected on the steel flange, laying a basis for constructing the reinforcement of concrete slab. With BSS as an example, the steel corrugated sleeves were employed to cover the shear studs and then fixed by iron wires to the nearby steel bars, serving as an isolation for external C50 concrete. To prevent external concrete leaking into the steel corrugated sleeve, a geotextile was stuffed into the sleeve and then rammed to the stud root with a steel bar for absorbing the cement slurry leaking at the bottom. Moreover, the sponge material was tied by iron wires to absorb the cement slurry leaking at the top. The external C50 concrete was cast after the leak-proof measure was completed. When the concrete was close to the initial set, a rebar with a bending hook was adopted to remove the geotextile out of the sleeve. On that basis, a multitude of small stud holes were created on the concrete slab. After 7 days, the concrete was finally set, and then small stud holes were cast with UHPC. Accordingly, the

concrete slab and the steel structure were integrated at a whole. Lastly, two identical parts were connected with bolts.

(**a**) Erect framework

(**b**) leak-proof measure

(**c**) Cast stud holes with UHPC

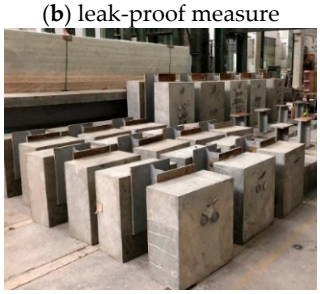

(**d**) Connect two parts at a whole

Figure 2. Construction process of BSS.

2.2. Material Properties

The cubic compressive strength, axial compressive strength, elastic modulus, and tensile strength possessed by C50 concrete and UHPC were tested. Moreover, the yield strength, ultimate tensile strength, and elastic modulus of the studs were examined. Table 2 lists the averaged test results.

Table 2. Material test results table (unit: MPa).

Concrete Properties	Cubic Compressive Strength	Axial Compressive Strength	Elastic Modulus ($\times 10^3$)
C50 Concrete	53.2	39.9	35.77
UHPC	136.8	129.4	44.00
Stud Properties	Yield Strength	Ultimate Tensile Strength	Elastic Modulus ($\times 10^3$)
ML15 Stud	367	486	217

2.3. Test Setup and Loading Programs

A total of four displacement transducers were strategically positioned around the steel–concrete interface to examine the relative slip between the stud root and the concrete slab, the arrangement of displacement transducers is shown in Figure 3.

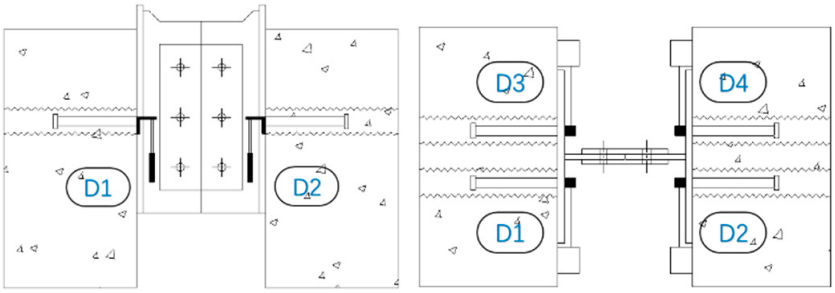

Figure 3. Arrangement of displacement transducers.

Figure 4 shows the experimental setup. The steel structure on the top of the specimens was loaded with a YAJ-10000 micro-controlled electro-hydraulic servo shear test machine, which is capable of exerting a maximum force of 10,000 kN. A steel pad was positioned on the top of the specimen, and a 6 mm rubber pad was arranged between the steel pad and the reaction frame, ensuring that the loading force was evenly distributed to the studs on both sides.

Figure 4. Experimental setup.

The specimens were pre-loaded three times at the estimated ultimate load of 20% before formal loading. The purpose of pre-loading was to examine the symmetry of the readings from the four displacement transducers. If any localized uneven loading was observed, the specimen was unloaded, and the steel plates on the top were re-leveled. In the practical loading process, a loading mode transition was reported at 60% of the estimated load. A force-controlled loading mode was employed, with a loading rate of 5 kN/s, in the first half of loading. In the latter half, a displacement-controlled loading mode was continuously employed with a loading rate of 0.5 mm/min until the specimen reached failure. Sampling was conducted at a frequency of 2 Hz.

3. Experimental Results

3.1. Failure Modes

Figure 5 presents the typical failure modes of the conventional stud push-out specimen OHS and the new bellow-sleeved stud push-out specimen BSS. In all specimens, the studs were sheared at their roots, accompanied by localized crushing of the concrete beneath the studs. As depicted in the figures, the UHPC at the root of the sleeved stud was partially exposed, and the steel sleeve beneath the stud was crushed under the effect of compression. Since the UHPC at the root of the sleeved stud exhibited a higher strength, the concrete failure region of the sleeved stud was slightly smaller than that of the ordinary stud. As indicated by the above results, in the testing process, BSS was primarily subjected to direct shear at its root, whereas OHS was more pronouncedly bent.

(**a**) (**b**) (**c**)

Figure 5. *Cont.*

(**d**) (**e**) (**f**)

Figure 5. Failure modes of push-out specimens. (**a**) Failure mode of OHS-a; (**b**) Concrete side of the failure face of OHS-a; (**c**) Steel structure side of the failure face of OHS-a; (**d**) Failure mode of BSS-a; (**e**) Concrete side of the failure face of BSS-a; (**f**) Steel structure side of the failure face of BSS-a.

3.2. Load–Slip Curves and Discussion

Figure 6 illustrates the load–slip curves plotted through the push-out tests. The horizontal axis represents the average slip for the respective specimen, i.e., the mean value of all displacement sensor readings. The vertical axis represents the average shear load per stud for the respective specimen. The load–slip curves with regard to specimens in the identical group exhibited a certain variability. Notably, the shear capacity of OHS-b was significantly higher than that of the other two specimens characterized by identical configurations. The remaining two specimens had relatively consistent load–slip curves. It is noteworthy that the load–slip curves for BSS possessed a slightly greater variability than those of OHS. This variability primarily arose from the effect on the metal corrugated sleeve when the concrete was being poured, such that the studs were off-center in the sleeve.

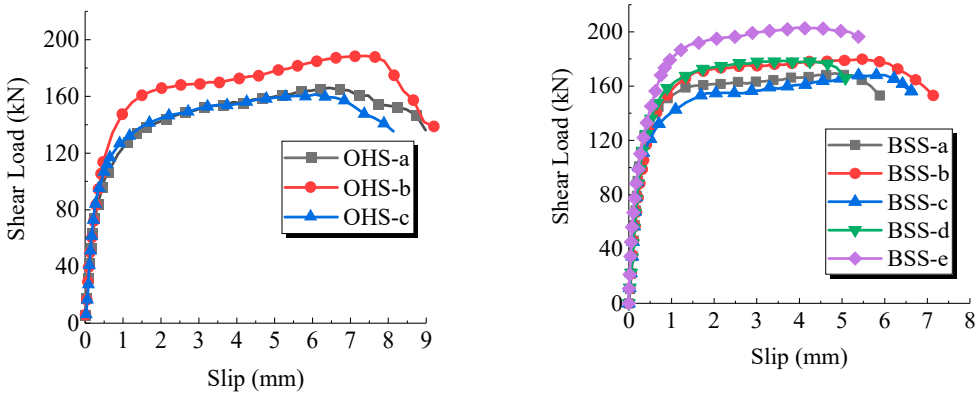

(**a**) Specimen OHS (**b**) Specimen BSS

Figure 6. Push-out test load–slip curve.

Although variability existed among specimens in the identical group, Figure 6 clearly presents the differences in shear performance between the two types of studs. BSS exhibited a higher ultimate shear capacity and shear stiffness than OHS, and a relatively small slip value corresponding to the ultimate load was generated.

Table 3 lists the summarized test results for the respective specimens. Here, V_u is the ultimate shear capacity of the studs, S_p is the slip at the ultimate shear capacity, and $K_{0.2mm}$, $K_{1/3}$, and $K_{1/2}$ denote the shear stiffness of the studs corresponding to the slip values of 0.2 mm, $1/3V_u$, and $1/2V_u$, respectively. This table lists the variations in shear performance for the respective specimens. Compared with OHS, BSS achieved an increase in the ultimate shear capacity by 4.5%, while the ultimate slip decreased by 27.7%. The above-mentioned results suggested that BSS did not confer an advantage over OHS in enhancing shear strength, whereas it exhibited a robust ability to resist slip deformation. Moreover, the shear stiffness of BSS increased by 31.9% compared with OHS.

Table 3. Summary of push-out test results.

Group	ID	Ultimate Shear Capacity V_u (kN)		Slip at Ultimate Shear Capacity S_p (mm)		Shear Stiffness $K_{0.2mm}$ (kN/mm)		Shear Stiffness $K_{1/3}$ (kN/mm)		Shear Stiffness $K_{1/2}$ (kN/mm)	
OHS	a	166.8	Avg: 172.6 0%	6.45	Avg: 6.67 0%	312	Avg: 329 0%	327	Avg: 333 0%	247	Avg: 272 0%
	b	189.7		7.45		331		321		266	
	c	161.3		6.90		342		351		313	
BSS	a	169.7	Avg: 180.3 ↑4.5%	4.59	Avg: 4.82 ↓27.7%	444	Avg: 434 ↑31.9%	422	Avg: 462 ↑38.7%	429	Avg: 402 ↑47.8%
	b	180.0		5.09		370		387		331	
	c	168.7		5.90		455		457		446	
	d	179.1		4.20		424		456		398	
	e	203.8		4.34		477		629		434	

4. Numerical Analysis

4.1. Overview

Finite-element models were built by Abaqus 2020 in terms of the push-out specimens OHS and BSS, and the relevant parameters were analyzed, so as to compare the shear performance of the new bellow-sleeved studs with that of conventional studs. Stud height, sleeve infill material, and sleeve diameter were the parameters analyzed. In accordance with the symmetry of the push-out specimens, only a quarter of the specimen was modeled in the finite-element analysis. The model is shown in Figure 7.

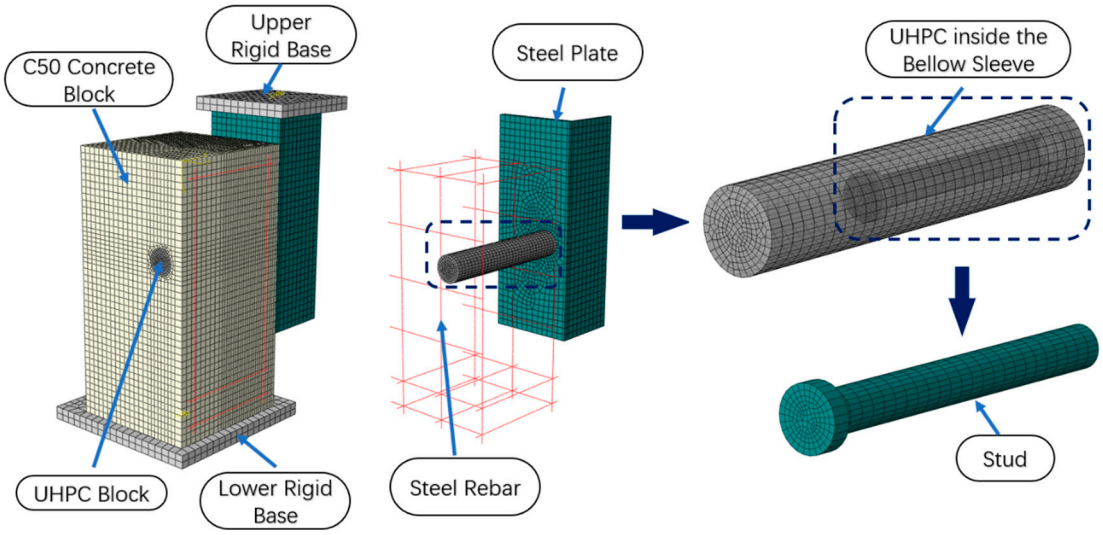

Figure 7. Abaqus finite-element model.

The model was constituted by concrete blocks, steel sleeves, steel plates, reinforcement mesh, and studs. The concrete block was made of two distinct materials, with UHPC arranged inside the sleeve and ordinary C50 concrete placed outside the sleeve. Moreover, the model covered two rigid bases on the top of the steel structure and the bottom of the concrete, and a reference point was placed at the center of the respective base to capture the push-out reaction force in the loading process. In the practical loading process, a displacement of 10 mm was applied to the reference point on the top base of the steel structure.

Concrete blocks, studs, and steel plates were represented using C3D8R solid elements, while steel rebars were modeled with T3D2 truss elements. The overall element size of the

specimen was 15 mm. To increase computational accuracy, the mesh was locally refined with a finer resolution of 3 mm around the studs and the steel plates.

4.2. Material Constitutions

(1) Concrete material constitutive model

Table 4 shows the material properties of concrete used in FEM analysis. The stress–strain relationship of the axial compression and tension of concrete can be simulated using the plastic damage model (CDP model) based on Abaqus 2020. This model quantifies the stiffness degradation of concrete in the nonlinear phase using the plastic damage factor d, which conforms to the energy equivalence principle proposed by Sidoroff.

Table 4. The material properties of concrete used in FEM analysis.

Concrete Material	Elastic Modulus E_c (GPa)	Axial Compressive Strength $f_{c,r}$ (MPa)	Ultimate Compressive Strain $\varepsilon_{c,r}$	Axial Tenile Strength $f_{t,r}$ (MPa)	Ultimate Tensile Strain $\varepsilon_{t,r}$
C50 Concrete	35.77	39.9	0.0017	2.7	0.00009
UHPC	44.00	129.4	0.0035	8.0	0.0002~0.002

The calculation of the nonlinear constitutive model was conducted through the following steps. With the compressive constitutive behavior of C50 as an example, the initial elastic modulus E_c = 35.77 GPa and axial compressive strength $f_{c,r}$ = 39.9 MPa were first obtained based on material testing. According to the method specified in GB 50010-2010 [21], the ultimate compressive strain $\varepsilon_{c,r}$ = 0.0017 was computed based on the damage factors d_c for different stages. In accordance with the above computation result, the stress–strain ($\sigma - \varepsilon$) curve was plotted in Figure 8. Subsequently, the process was divided into two segments for input into the software. In the initial linear segment, only the initial elastic modulus and axial compressive strength should be input. With regard to the nonlinear segment, non-elastic strains $\tilde{\varepsilon}_c^{in}$ for each stage were calculated (tensile cracking strain is expressed as $\tilde{\varepsilon}_c^{in}$). In accordance with the Sidoroff energy equivalence principle, the corresponding damage factor d was derived. Lastly, the stress σ_c to non-elastic strain $\tilde{\varepsilon}_c^{in}$ relationship and the damage factor d to non-elastic strain $\tilde{\varepsilon}_c^{in}$ relationship were imported into Abaqus 2020 software as the constitutive model for concrete.

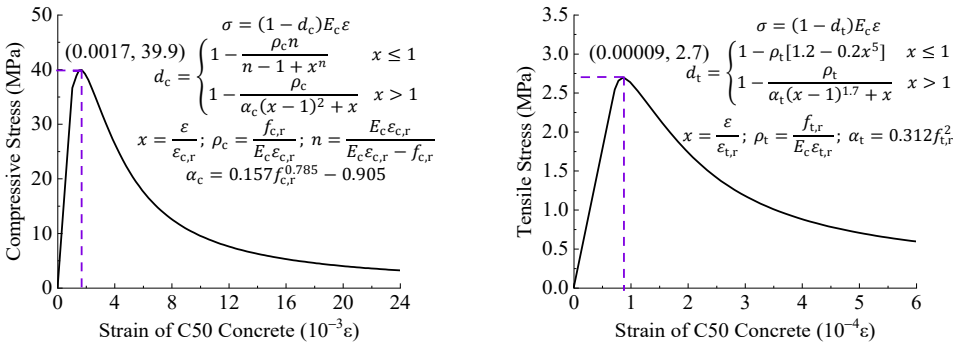

(**a**) Compressive stress (**b**) Tensile stress

Figure 8. Constitutive model of C50 concrete.

The input method for the constitutive model of UHPC is identical to that for C50 concrete, and the constitutive curve is plotted in Figure 9. For the compressive constitutive model, f_c represents the examined axial compressive strength, with a value of 129.4 MPa. The ultimate compressive strain $\varepsilon_{c.r}$ was taken as 0.0035, and the initial elastic modulus E_c was assigned a value of 44.0 GPa based on the material testing results. E_s represents the

secant modulus at the stress peak point. For the tensile constitutive model, f_{ct} was assigned a value of 8.0 MPa, and the strain values for the peak point ε_{ca} and the ultimate point ε_{pc} were computed as 0.0002 and 0.002, respectively. The parameter α principally affected the descending segment, and it was set at 1.106 based on the characteristics of the steel fibers.

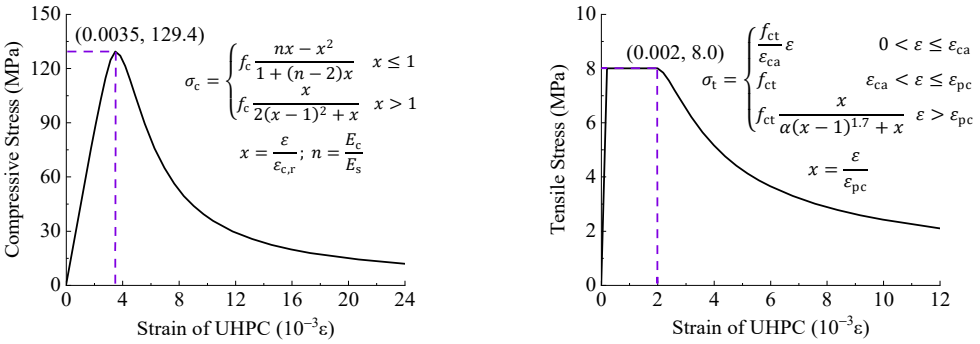

(**a**) Compressive stress (**b**) Tensile stress

Figure 9. Constitutive model of UHPC.

(2) Steel material constitutive model

Table 5 shows the material properties of steel used in FEM analysis. The stress–strain curve of the stud material is expressed by the three-segment model as illustrated in Figure 10a. The yield stress and ultimate stress of the material were first derived based on the material testing results and then converted into the corresponding true stresses, where were measured at 368 MPa and 498 MPa, respectively. The ultimate strain was set at 2.5%, and the elastic modulus was computed as 207 GPa. The stress–strain curves for steel materials and steel bars were modeled using the dual-segment model, as depicted in Figure 10b. The yield stresses for steel materials and steel bars were obtained as 345 MPa and 400 MPa, respectively, and the elastic modulus was set at 206 GPa.

Table 5. The material properties of steel used in FEM analysis.

Steel Material	Elastic Modulus (GPa)	Yield Strength (MPa)	Ultimate Strength (MPa)
Stud	207	367	486
Steel Plate	206	345	345
Steel Rebar	206	400	400

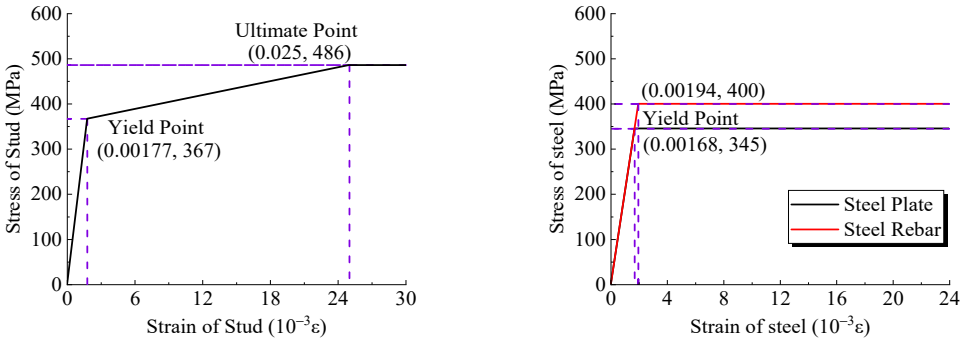

(**a**) Constitutive model of stud (**b**) Constitutive model of steel plate and rebar

Figure 10. Constitutive model of steel material.

4.3. Boundary Condition

The model with regard to the boundary condition employs surface-to-surface contact to simulate the interactions among the steel–concrete interface, C50–UHPC interface, and

UHPC–stud contact. Tangential contact was simulated with the penalty function friction formula, while normal contact was modeled as hard contact. Since lubricating oil was applied to the steel–concrete interface in the push-out test, the friction coefficient for this interface was set at 0.01. The friction coefficient between UHPC and the stud was set at 0.2. A corrugated metal sleeve with a thickness of 0.6 mm was present between C50 and UHPC, creating a waviness at their interface and generating a higher friction coefficient of 0.6. The interaction between steel reinforcement and concrete was constrained using the embedded command. The upper and lower rigid bases were connected to the surfaces of the specimen with the Tie command.

Figure 11 illustrates the boundary conditions of the model. As the model represents only 1/4 of the practical push-out specimen, appropriate constraints on the surface were applied to the symmetric planes. Furthermore, the frictional interaction between the bottom surface of the concrete block and the test platform was not considered in this model, assuming a complete fixation between the concrete block and the test platform.

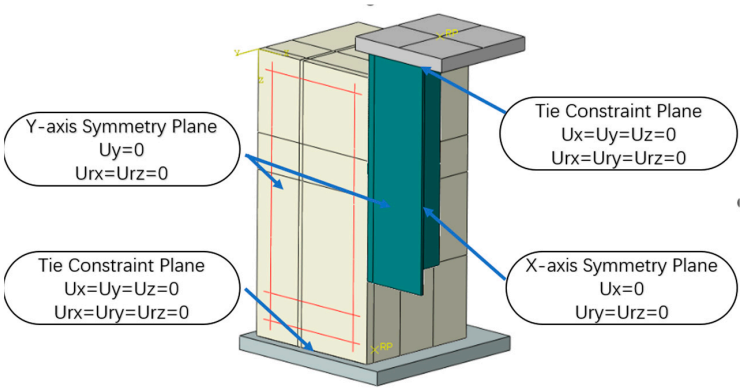

Figure 11. Schematic of model boundary conditions.

4.4. Simulation Verification

(1) Load–Slip curves

Figure 12 presents the comparison between numerically simulated load–slip curves and the results from the push-out tests. The simulated curves are well consistent with the experimental curves. Since the simulation did not explain the stud material damage, the differences in the elastic phase were minor for BSS. However, in the nonlinear phase, the load-bearing capacity was overestimated to a certain extent. Table 6 compares the key shear parameters obtained from the simulation and average test results, revealing discrepancies of 2% to 13%. The above-mentioned differences were primarily attributed to external factors (e.g., sleeve eccentricity, grout leakage at the bottom, and welding quality). In general, the numerical model was validated to have rationality and consistency with the experimental model, effectively capturing the shear characteristics of the studs.

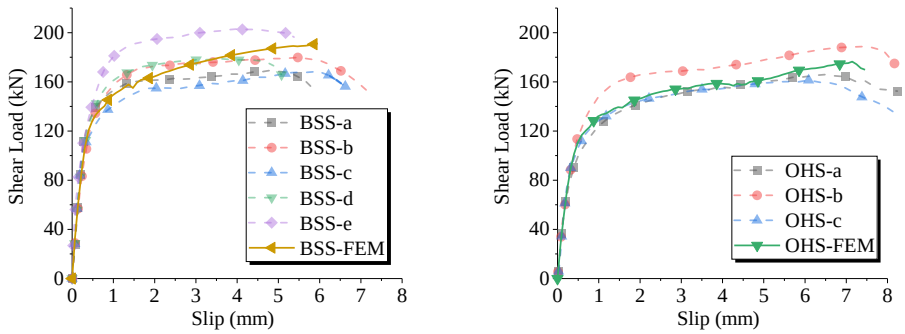

(**a**) BSS (**b**) OHS

Figure 12. Model validation.

Table 6. Comparison of shear parameters between experiments and FEM models.

Group	Ultimate Shear Capacity V_u (kN)		Shear Stiffness $K_{1/3}$ (kN/mm)		Shear Stiffness $K_{1/2}$ (kN/mm)	
BSS-AVG	180.3	↓6%	462	↑13%	402	↑11%
BSS-FEM	191	0%	410	0%	361	0%
OHS-AVG	172.6	↓2%	333	↑3%	272	↓4%
OHS-FEM	176	0%	323	0%	284	0%

(2) Failure mode

The current model cannot simulate the process of stud fracture for not incorporating the metallic damage of the studs. Thus, the moment when the shear capacity reaches its peak serves as the comparative benchmark for the ultimate failure mode. Figure 13 presents the compressive damage distribution of the concrete and Mises stress distribution of the studs that was derived through the finite-element simulation at the ultimate state. As depicted in the figure, the extent of concrete damage in BSS was slightly smaller than that in OHS. Since the damage factor of UHPC was only defined up to 0.7, the internal part of the sleeve, presented by the lighter color, was subjected to greater damage, well consistent with the practical photographs of the failure mode. The comparison of the stress distribution of the studs suggested that the Mises stress contours of BSS were similar to those of OHS. However, the deformation pattern at the root of the studs was pronouncedly distinct. BSS displayed angular deformation at its root, and the overall bending deformation was less pronounced than that of the OHS. The above results suggested that BSS was subjected to less bending–shear coupling, exhibiting a superior shear performance.

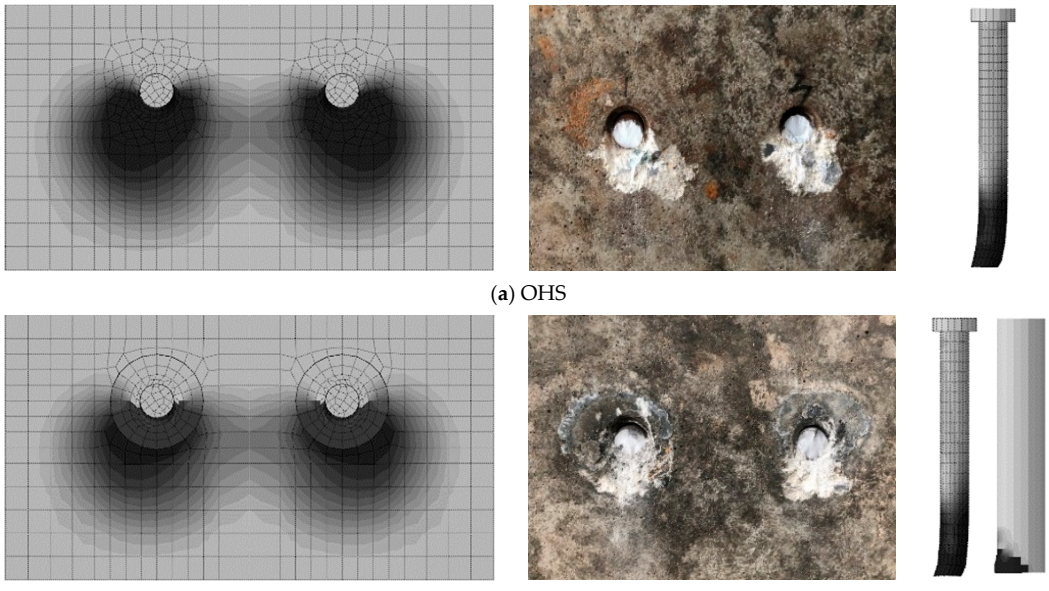

(**a**) OHS

(**b**) BSS

Figure 13. Comparison of failure modes.

4.5. Stress Analysis

(1) Axial normal stress

The axial stresses on the upper and lower edges of the studs in the models for BSS and OHS were extracted, as presented in Figure 14, to investigate the stress distribution along the body of the stud in the loading process. The approximately symmetric axial stresses were imposed on the upper and lower edges of the two studs. With the upper edge of the stud as an example, the upper edge near the root location was subjected to compressive

stresses. However, as the height increased, the compressive stress rapidly declined and shifted to tensile stress with a height of nearly 15 mm. At a height of about 35 mm, the stress reached a peak tensile stress and then tended to decline, nearly approaching 0 MPa around 95 mm in height, suggesting a stabilized state. In contrast, the distribution of axial stresses on the lower edge of the stud displayed the opposite pattern. The bending behavior of the stud was indicated by the difference between the upper and lower edge axial stresses. As depicted in the figure, the axial stresses on the upper and lower edges of the stud were almost equal beyond a height of 95 mm, suggesting that the longitudinal loading characteristics of the stud contained bending stresses primarily at a height of 95 mm from the root. However, beyond this height, they were largely subjected to axial tensile forces.

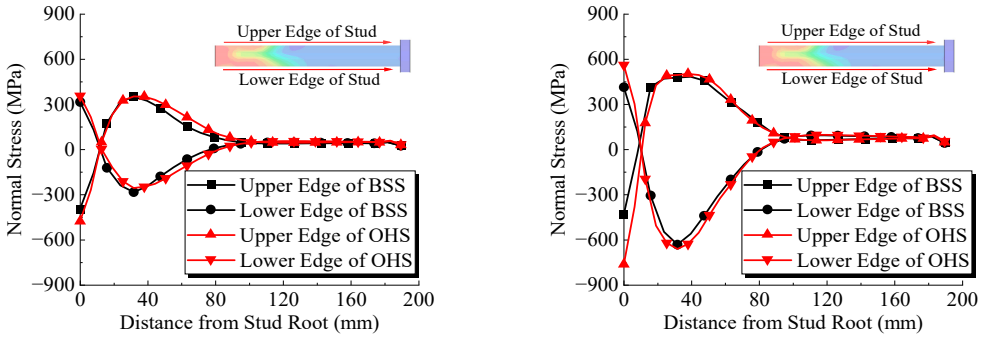

(**a**) 50%V_u (**b**) 90%V_u

Figure 14. Stud normal stress distribution.

As revealed by the further comparison of the axial stress distributions for both types of stud connections at different loading stages, under the shear load of 50%V_u, a minor difference was found in axial stresses between the two types of studs, while BSS had a slightly lower axial stress. However, under the shear load of 90%V_u, the axial stresses of the two studs differed significantly in 15 mm from the root. The axial stress in BSS was approximately 30% to 40% lower than that in OHS, suggesting a weaker degree of bending at the root. The above finding corroborated the conclusions drawn from the observed failure mode. Furthermore, the stress distributions on both types of studs at a height of 15 mm were almost consistent, with similar peak stress values.

(2) Shear stress

The stress displayed a highly complex distribution at the root of the stud during the push-out test. Apart from normal stresses induced by bending and tension, shear stresses were also generated under the effect of direct shear action. Figure 15 presents the numerical extraction of shear stresses along the height direction of the stud's central axis. As depicted in the figure, the shear stress distribution was similar for both types of studs, and peak shear stresses were found at the root of the studs, reaching approximately 280 MPa.

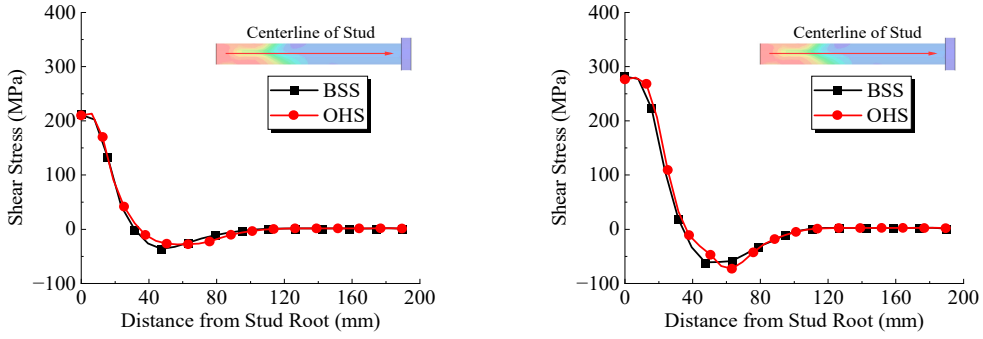

(**a**) 50%V_u (**b**) 90%V_u

Figure 15. Stud shear stress distribution.

Since the shear force was the first derivative of the bending moment, when the distance from the root ranged from 0 mm to 15 mm, the shear stress continued to be high, whereas the normal stresses rapidly varied at this interval. As the distance from the root increased from 15 mm to 35 mm, the shear stress crossed 0 and reversed direction, such that normal stresses achieved reversed peak values that tended to decrease. In the range of 35 mm to 95 mm from the root, the reversed shear stress first increased and then gradually decreased to 0, while the normal stresses also declined gradually and stabilized at a certain level. It can be inferred from the aforementioned analysis that in the range of 35 mm from the root, the stud's lower edge concrete contributed to the shear resistance. Moreover, in the range of 35 mm to 95 mm, the upper edge concrete of the stud contributed to shear resistance. It is noteworthy that the concrete below the stud is critical in providing shear resistance, while it is inevitably subject to compression failure at the ultimate state. When compared with OHS, the reversed shear peak of BSS was closer to the root, suggesting that a more pronounced direct shear effect was generated.

5. Parametric Analysis

5.1. Concrete Material Type for BSS

A total of five finite-element models of the pull-out tests were developed using a wide variety of concrete materials to compare the differences in shear performance between BSS and OHS. The model numbering complied with the rule "base model—sleeve outer material—sleeve inner material". For OHS without sleeves, the concrete materials were comprised of C50 and UHPC. For BSS with sleeves, the computed models consider the economical combination "C50–C50" and the commonly used combination "C50–UHPC", as well as the combination used for UHPC bridge decks "UHPC–UHPC". Figure 16 presents the load–slip curves of different stud connections, and Table 7 summarizes the shear performance indicators. The results of OHS-C were employed as the benchmark for comparison.

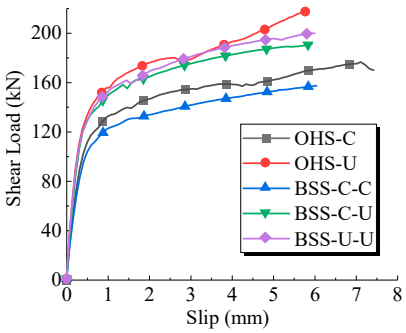

Figure 16. Load–slip curves of stud connectors with different materials.

Table 7. Effect of concrete material type on shear performance of BSS and OHS.

Model Number	Concrete Material Type		Ultimate Shear Capacity V_u (kN)		Shear Stiffness $K_{1/3}$ (kN/mm)		Shear Stiffness $K_{1/2}$ (kN/mm)	
	Outside Sleeve	Inside Sleeve						
OHS-C	C50	N/A	176	0%	323	0%	284	0%
OHS-U	UHPC	N/A	218	↑24%	445	↑38%	367	↑29%
BSS-C-C	C50	C50	152	↓14%	299	↓7%	268	↓6%
BSS-C-U	C50	UHPC	191	↑8%	410	↑27%	361	↑27%
BSS-U-U	UHPC	UHPC	200	↑14%	438	↑36%	372	↑31%

As indicated by the computed results, the shear capacity of BSS-C-C was 24% lower than OHS-C, and the shear stiffness declined by 7%. Likewise, BSS-U-U possessed a shear capacity 10% lower than OHS-U and a shear stiffness decrease of only 3%. The above results

suggested that incorporating the steel corrugated sleeve in the concrete led to the reduced overall integrity of the concrete block, reducing the shear performance indicators of the stud. Moreover, the shear strength and stiffness of the concrete materials with lower performance characteristics more pronouncedly decreased. To address the decrease in the shear capacity, BSS-C-U has been generally adopted in engineering practice, which was the bellow-sleeved stud employed in this pull-out test. After UHPC was infused into the sleeve, the shear capacity was improved by approximately 8%, and the shear stiffness was improved by 27%. Superior material performance can be exploited to overcome the shortcomings in construction. Accordingly, in practical bridge design, the steel sleeve should not be filled with ordinary concrete containing fine aggregates. Instead, it is necessary to use a higher modulus of elasticity and better flowability materials (e.g., high-strength mortar or UHPC).

5.2. Stud Height

Due to limitations in the number of specimens, the experimental process only tested the commonly used ML15 studs with a diameter of 22 mm and a height of 200 mm in bridge engineering. There was no comparison made regarding the effect of the aspect ratio (height-to-diameter ratio) on the shear performance of BSS. In this section, finite-element models were established for studs of different heights, ranging from 80 mm to 250 mm. This corresponds to an aspect ratio range of 3.6 to 11.4. The model numbering follows the rule "base model—H stud height". Figure 17 analyzes the variation in shear stiffness of BSS with variations in stud length, and Table 8 presents the computed results of the simulation with varying stud heights. The baseline model is designated as BSS-H200.

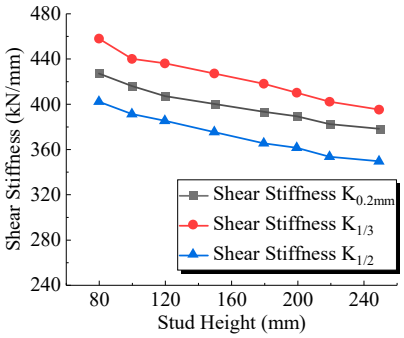

Figure 17. Effect of stud height variation on shear stiffness.

Table 8. Effect of stud height on the shear performance of BSS.

Model Number	Stud Height (mm)	Ultimate Shear Capacity V_u (kN)		Shear Stiffness $K_{1/3}$ (kN/mm)		Shear Stiffness $K_{1/2}$ (kN/mm)	
BSS-H80	80	199	↑4%	458	↑12%	402	↑11%
BSS-H100	100	198	↑4%	440	↑7%	391	↑8%
BSS-H120	120	191	0%	436	↑6%	385	↑7%
BSS-H150	150	192	↑1%	427	↑4%	375	↑4%
BSS-H180	180	192	↑1%	418	↑2%	365	↑1%
BSS-H200	200	191	0%	410	0%	361	0%
BSS-H220	220	190	↓1%	402	↓2%	353	↓2%
BSS-H250	250	189	↓1%	395	↓4%	349	↓3%

The computed results indicate that as the height of the stud increases, the shear strength and shear stiffness show a slight decreasing trend. However, the magnitude of this variation is small, suggesting that the shear behavior of the stud primarily occurs at the root, and its relationship with height is relatively minor. Previous studies have shown that the conventional stud exhibits a coupling of bending and shearing in pull-out tests. As the stud height increases, the bending effect becomes more prominent, leading to a decrease in shear performance. However, in this simulation, UHPC near the root of the sleeved stud

has a higher stiffness, resulting in less bending of the stud. Thus, the simulation results are less sensitive to variations in stud height.

Additionally, when the aspect ratio of the stud is less than 4, the shear performance of the stud significantly improves. The shear capacity increases by 4%, and the shear stiffness increases by approximately 11%. When the aspect ratio is between 5 and 11, the shear performance of the stud remains relatively stable, with variations within 4% for all performance indicators. This indirectly indicates that the current design codes have certain limitations on the aspect ratio of studs. In this range, BSS can be uniformly calculated using the prescribed formulas.

5.3. Sleeve Diameter and Stud Diameter

In this study, the commonly used outer diameter 60 mm corrugated metal sleeve was chosen as the steel sleeve for the studs, and no experimental tests were conducted on sleeves of other specifications. Additionally, the effect of the stud diameter and sleeve diameter on the shear performance was not investigated. To address this, finite-element models were developed for sleeves with different diameters (ranging from 50 mm to 90 mm) and varying stud diameters (19 mm, 22 mm, 25 mm). The model numbering convention is "base model—R stud diameter—D sleeve diameter." The computed results are presented in Table 9, and the comparison is based on their respective D60 models.

Table 9. Effect of sleeve diameter on the shear performance of BSS.

Model Number	Ultimate Shear Capacity V_u (kN)		Shear Stiffness $K_{1/3}$ (kN/mm)		Shear Stiffness $K_{1/2}$ (kN/mm)	
BSS-R19-D50	153	↓3%	347	↓1%	302	↓2%
BSS-R19-D60	159	0%	351	0%	307	0%
BSS-R19-D70	164	↑3%	373	↑6%	318	↑4%
BSS-R19-D80	168	↑6%	387	↑10%	318	↑4%
BSS-R19-D90	169	↑6%	403	↑15%	331	↑7%
BSS-R22-D50	186	↓3%	385	↓6%	349	↓3%
BSS-R22-D60	191	0%	410	0%	361	0%
BSS-R22-D70	196	↑3%	415	↑1%	369	↑2%
BSS-R22-D80	206	↑8%	436	↑6%	374	↑4%
BSS-R22-D90	207	↑8%	447	↑9%	380	↑5%
BSS-R25-D50	222	↓3%	443	↓3%	402	↓3%
BSS-R25-D60	228	0%	455	0%	414	0%
BSS-R25-D70	236	↑4%	475	↑4%	426	↑3%
BSS-R25-D80	246	↑8%	474	↑4%	423	↑2%
BSS-R25-D90	250	↑10%	481	↑6%	430	↑4%

Figure 18a,b depict the variations in shear capacity and shear stiffness with variations in steel sleeve diameter under three stud diameters, respectively. It can be observed that as the sleeve diameter increases, the shear strength and shear stiffness of the stud also increase, suggesting that the UHPC inside the sleeve provides a stronger resistance against the bending and shearing of the stud. When comparing models with the same stud diameter, as the sleeve diameter exceeds 80 mm, the rate of increase in shear capacity slows down and approaches a critical point, while the rate of increase in shear stiffness remains unchanged. Although the simulation results demonstrate that larger sleeve diameters lead to a better shear performance of BSS, effectively mitigating the negative effect of the steel sleeve, practical bridge engineering considerations, such as the group arrangement of studs, spatial limitations, and rebar clearances, suggest that the sleeve diameter should not exceed 70 mm. For sleeve diameters of 50 mm to 70 mm, the shear capacity and shear stiffness vary within ±3%. Thus, when designing connections in this range, it may not be necessary to account for the effect of sleeve diameter variation on shear performance.

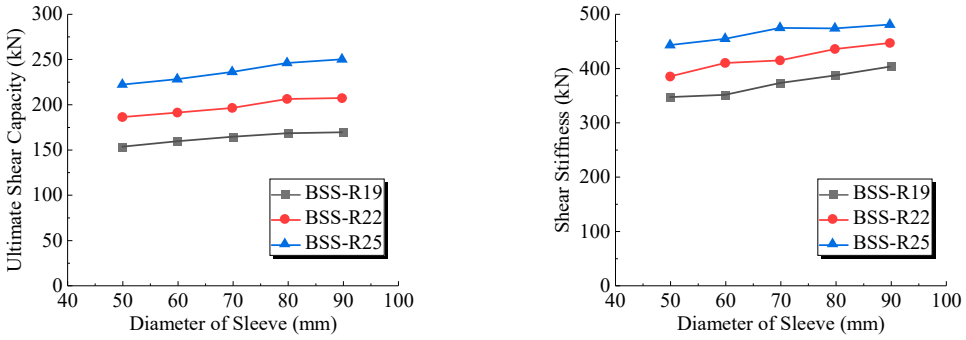

(**a**) ultimate shear capacity (**b**) shear stiffness

Figure 18. Variation curve of shear parameters with sleeve diameter.

Comparing the differences in the shear performance of BSS under various stud diameters, from the perspective of shear capacity, larger stud diameters are more significantly affected by the sleeve diameter. The shear capacity of the stud with a 25 mm diameter fluctuates from −3% to 10%, while that of the 19 mm-diameter stud varies within −3% to 6%. Considering shear stiffness, larger stud diameters are less influenced by sleeve diameter. The shear stiffness of the 25 mm-diameter stud varies within −3% to 6%, while that of the 19 mm-diameter stud even exceeds 10%. From these observations, the shear stiffness of the larger diameter stud is more correlated with the material properties of the stud itself, with the contribution of the concrete material strength to shear stiffness being relatively smaller. As a result, the effect of sleeve diameter variation is relatively minor.

5.4. Deviation of Sleeve and Stud Relative Position

During the course of the experiment, significant variability was observed in the results of BSS. This variation was attributed to certain specimens where the steel sleeve deviated due to the effect of concrete during pouring, causing the stud to be off-center in the sleeve. As a result, the concrete material properties around the root of the stud exhibited considerable differences. To address this issue, finite-element models were developed for specimens with four different positions of the steel sleeve, investigating the effect of a 1 cm deviation in the stud position in the sleeve. The model numbering convention is "base model—position of stud relative to sleeve interior (up—stud positioned higher, down—stud positioned lower, side—stud positioned at the side)", with BSS-middle serving as the comparative baseline.

The load–slip curves of the models are depicted in Figure 19, and shear performance indicators are presented in Table 10. The simulation results indicate that the positioning of the stud inside the sleeve, whether higher or lower, has a significant effect on the shear performance. When the stud is positioned higher, the shear capacity increases by 5%, and the shear stiffness by 7%. In this scenario, there is a thicker UHPC layer below the root of the stud to withstand the compressive stress transmitted from the lower surface of the stud. Conversely, when the stud is positioned lower, the shear capacity decreases by 5%, and the shear stiffness decreases by 13%. This is attributed to the thinner UHPC layer beneath the root of the stud, coupled with its closer proximity to the weakened section near the corrugated sleeve wall, resulting in unfavorable loading conditions. In the case of a sidewise deviation, there is minimal variation in the ultimate shear capacity, and the shear stiffness slightly decreases by 1%. In summary, it can be concluded that the deviation of the sleeve position has a relatively small and symmetric effect on shear capacity, while its influence on shear stiffness is more pronounced.

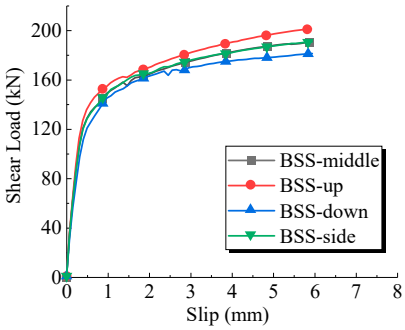

Figure 19. Load–slip curves of BSS with different sleeve positions.

Table 10. Effect of sleeve installation deviation on the shear performance of BSS.

Model Number	Sleeve Installation Deviation	Ultimate Shear Capacity V_u (kN)		Shear Stiffness $K_{1/3}$ (kN/mm)		Shear Stiffness $K_{1/2}$ (kN/mm)	
BSS-middle	Stud Centered	191	0%	410	0%	361	0%
BSS-up	Stud 1 cm Above Center	201	↑5%	435	↑6%	388	↑7%
BSS-down	Stud 1 cm Below Center	181	↓5%	358	↓13%	314	↓13%
BSS-side	Stud 1 cm to the Side	191	0%	406	↓1%	356	↓1%

5.5. Sleeve Grout Leakage Height

During construction, notwithstanding the effect of sleeve deviation, the leakage of grout at the bottom of the sleeve can adversely affect the shear performance of BSS. Grout leakage can reduce the material strength of the concrete surrounding the root of the stud, leading to the premature compressive failure of the concrete. Although measures were taken to prevent leakage in the current experimental tests, since there were no cases of grout leakage, the reality of construction sites with a large number of stud connections cannot ensure the construction quality of leakage-proof measures, inevitably resulting in some degree of grout leakage in the sleeve. Once the grout fills the root of the stud, it can adversely affect the shear performance of the connection. Thus, finite-element models were developed for stud specimens with different degrees of grout leakage in the sleeve. The grout leakage height ranged from 10 mm to 50 mm, assuming that the grout material in the sleeve is C50 concrete, with UHPC remaining above the grout leakage. The model naming convention is "base model—grout leakage height", with BSS-C-U as the baseline model.

Table 11 summarizes the shear performance parameters for each model. Figure 20 depicts the load–slip curves for each model. BSS-C-U represents the model with no grout leakage and essentially serves as the upper limit of the curves, while BSS-C-C represents the model with C50 concrete filling in the sleeve and acts as the lower limit of the curves. The other curves lie between these two scenarios. A comparison of models with grout leakage reveals that grout failure around the root of the studs occurs prematurely, leading to a sharp decrease in shear load. Although the shear load still increases after the grout failure, it cannot exceed the maximum value before failure. Under the premature failure of the grout, a smaller ultimate slip displacement is generated, and the shear capacity develops insufficiently. For instance, with a grout leakage height of 50 mm, the maximum shear strength was reduced by approximately 16%. Figure 21 illustrates the effect of the grout leakage height on shear stiffness, showing a steep decline of about 22% when the leakage height ranged from 0 mm to 50 mm. When the leakage height went beyond 50 mm, the effect gradually declined, with the curve's shape resembling the deformation of the stud.

In brief, grout leakage in the sleeve can reduce the shear strength and shear stiffness of the stud connection. In practice, if proper measures were taken to prevent leakage, with the grout leakage height ensured to be within 10 mm, the effect on the capacity and stiffness was minor. If the grout leakage height exceeded 10 mm, subpar construction quality was

indicated, requiring the absorption of cement slurry leaking from the bottom of the sleeve using a geotextile fabric.

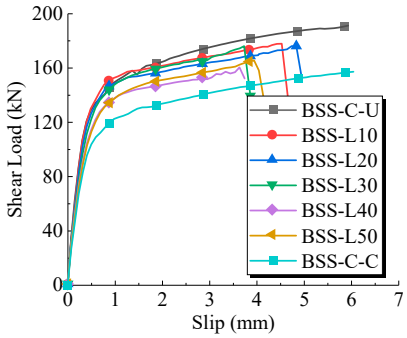

Figure 20. Load–slip curves of BSS with different grout leakage heights.

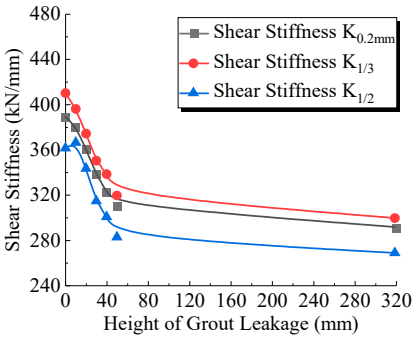

Figure 21. Effect of grout leakage height on shear stiffness.

Table 11. Effect of grout leakage height inside the sleeve on the shear performance of BSS.

Model Number	Grout Height Inside Sleeve (mm)	Ultimate Shear Capacity V_u (kN)		Shear Stiffness $K_{1/3}$ (kN/mm)		Shear Stiffness $K_{1/2}$ (kN/mm)	
BSS-C-U	0	191	0%	410	0%	361	0%
BSS-L10	10	178	↓7%	396	↓3%	366	↑1%
BSS-L20	20	176	↓8%	374	↓9%	343	↓5%
BSS-L30	30	176	↓8%	350	↓15%	314	↓13%
BSS-L40	40	160	↓16%	338	↓18%	300	↓17%
BSS-L50	50	166	↓13%	319	↓22%	282	↓22%
BSS-C-C	320	152	↓20%	299	↓27%	268	↓26%

6. Conclusions

In this study, BSS and OHS were investigated through push-out tests and numerical simulations. Next, the shear performance of these connections was compared. Moreover, the effect of different parameters and construction conditions on the shear performance of BSS was investigated. The conclusions of this study are drawn as follows:

(1) BSS and OSS exhibited shear failure at the root of the studs. The concrete damage region close to the root of BSS was smaller, and the bending deformation turned out to be less pronounced compared with OHS. As indicated by the above result, BSS was subjected to a greater effect of direct shear and a smaller effect of bending–shear coupling, exhibiting a superior shear performance.

(2) It is noteworthy that the steel corrugated sleeve of BSS led to the reduced overall integrity of the concrete block and declining shear performance indicators. Nevertheless, this deficiency in the structural design can be compensated by filling the steel corrugated sleeve with high-performance concrete materials (e.g., UHPC or high-strength mortar), such that superior material properties are exploited.

(3) The results of the push-out tests and numerical simulations confirmed that BSS exhibited a higher ultimate shear bearing capacity and larger shear stiffness than OHS. Moreover, the slip at the ultimate bearing capacity was minor. BSS did not confer advantages over OHS in enhancing shear strength, with a modest 4.5% increase in the ultimate shear capacity. However, BSS exhibited a strong resistance to slip deformation, with the shear stiffness increasing from 31.9%.

(4) Compared with the stud height, the sleeve diameter and the stud diameter significantly affected the shear capacity and stiffness of BSS. When the sleeve diameter varied from 50 mm to 100 mm, the shear strength and the shear stiffness increased by approximately 8% and 10%, respectively. As indicated by the above results, the UHPC near the root of the stud provided stronger shear support. Under the effect of the reinforcement arrangement in the bridge deck, the diameter of the corrugated sleeve should not exceed 70 mm to ensure sufficient reinforcement spacing.

(5) The sleeve deviation slightly affected the shear bearing capacity and showed symmetric characteristics. However, it significantly affected the shear stiffness, especially when the stud was positioned below the central axis of the sleeve. The leaking grout at the sleeve bottom exerted a more pronounced effect. When the grout leakage height fell into a range of 50 mm, the shear bearing capacity and the shear stiffness decreased by 16% and 22%, respectively. Thus, the installation quality of the corrugated steel sleeves should be tested rigorously.

Author Contributions: Methodology, D.Z.; Software, D.Z.; Validation, Q.S.; Formal analysis, D.Z.; Investigation, F.W.; Resources, F.W. and Z.L.; Data curation, P.L. All authors have read and agreed to the published version of the manuscript.

Funding: This research is sponsored by the Fujian Transportation Technology Project (No. 202126) and Henan Major Research and Development Program for Special Projects (No. 231111241500).

Data Availability Statement: The original contributions presented in the study are included in the article, further inquiries can be directed to the corresponding authors.

Conflicts of Interest: Author Zhiping Lin was employed by the company Fujian Expressway Group Co., Ltd. Author Peiran Li was employed by the company Henan Transportation Planning and Design Research Institute Co., Ltd. The remaining authors declare that the research was conducted in the absence of any commercial or financial relationships that could be construed as a potential conflict of interest.

References

1. Ollgaard, J.G.; Slutter, R.G.; Fisher, J.W. Shear strength of stud connectors in lightweight and normal weight concrete, AISC Eng'g Jr., April 1971 (71-10). *AISC Eng. J.* **1971**, 55–64.
2. Viest, I.M. Investigation of Stud Shear Connectors for Composite Concrete and Steel T-Beams. *J. Am. Concr. Inst.* **1956**, *27*, 875–891. [CrossRef] [PubMed]
3. Oehlers, D.J.; Coughlan, C.G. The shear stiffness of stud shear connections in composite beams. *J. Constr. Steel Res.* **1986**, *6*, 273–284. [CrossRef]
4. Prakash, A.; Anandavalli, N.; Madheswaran, C.K.; Lakshmanan, N. Modified push-out tests for determining shear strength and stiffness of HSS stud connector-experimental study. *Int. J. Compos. Mater.* **2012**, *2*, 22–31. [CrossRef]
5. Oehlers, D.J.; Foley, L. The fatigue strength of stud shear connections in composite beams. *Proc. Inst. Civ. Eng. Part Res. Theory* **2015**, *79*, 349–364. [CrossRef]
6. Roik, K.; Hanswille, G.; Cunze-O Lanna, A. *Harmonisation of the European Construction Codes*; Report of Eurocode; Ministerium fur Raumordnung, Bauwesen und Städtebau: Bonn, Germany, 1989.
7. *EN 1990*; Eurocode—Basis of structural design. Section 6 Verification by the Partial Factor Method. European Committee for Standardization: Brussels, Belgium, 2002.
8. *EN 1994*; Eurocode-4: Design of Composite Steel and Concrete Structures. Part 1-1 General Rules for Buildings. CEN-European Committee for Standardization: Brussels, Belgium, 2004.
9. *AASHTO LRFD Bridge Design Specifications*, 3rd ed.; American Association of State Highway and Transportation Officials: Washington, DC, USA, 2004.
10. *GB50017-2003*; Code for Design of Steel Structures. Ministry of Construction of China, China Planning Press: Beijing, China, 2003.

11. Roik, K. *Methods of Prestressing Continuous Composite Girders*; Proceedings, Conference on Steel, June 1968; BSSA: London, UK, 1969.
12. Ayyub, B.M.; Sohn, Y.G.; Saadatmanesh, H. Prestressed Composite Girders. I: Experimental Study for Negative Moment. *J. Struct. Eng.* **1992**, *118*, 2743–2762. [CrossRef]
13. Ayyub, B.M.; Sohn, Y.G.; Saadatmanesh, H. Prestressed Composite Girders. II: Analytical Study for Negative Moment. *J. Struct. Eng.* **1992**, *118*, 2763–2782. [CrossRef]
14. Chen, S. Experimental study of prestressed steel–concrete composite beams with external tendons for negative moments. *J. Constr. Steel Res.* **2005**, *61*, 1613–1630. [CrossRef]
15. Su, H.; Su, Q.; Xu, C.; Zhang, X.; Lei, D. Shear performance and dimension rationalization study on the rubber sleeved stud connector in continuous composite girder. *Eng. Struct.* **2021**, *240*, 112371. [CrossRef]
16. Xu, X.; Liu, Y.; He, J. Study on mechanical behavior of rubber-sleeved studs for steel and concrete composite structures. *Constr. Build. Mater.* **2014**, *53*, 533–546. [CrossRef]
17. Su, Q.; Yang, G.; Wu, C. Experimental studies on mechanical behavior of continuous composite girder with prefabricate prestressed concrete slab. *J. Tongji Univ.* **2012**, *40*, 996. [CrossRef]
18. Xue, D.; Liu, Y.; Yu, Z.; He, J. Static behavior of multi-stud shear connectors for steel-concrete composite bridge. *J. Constr. Steel Res.* **2012**, *74*, 1–7. [CrossRef]
19. Yu, J.; Wang, Y.H.; Liu, J.-P.; Chen, Y.F.; Xue, S.-L.; Yu, Z. Stiffness analysis of shear stud group connectors in precast concrete deck. *Eng. Struct.* **2023**, *274*, 115148. [CrossRef]
20. Su, Q.; Zou, D.; Zhang, L.; Tao, X.; Huang, C. Field Test and Effect Analysis of Concrete Prestress for the Post-Combined Prestressing Composite Girder Bridge. *J. Tongji Univ.* **2021**, *49*, 1061–1069. [CrossRef]
21. *GB50010-2010*; Code for Design of Concrete Structures. Ministry of Construction of China, China Planning Press: Beijing, China, 2010.